ALMA MATER STUDIORUM
UNIVERSITÀ DI BOLOGNA

ARCHIVIO ISTITUZIONALE
DELLA RICERCA

Alma Mater Studiorum Università di Bologna
Archivio istituzionale della ricerca

Exploring the capabilities of optical pump X-ray probe NEXAFS spectroscopy to track photo-induced dynamics mediated by conical intersections

This is the final peer-reviewed author's accepted manuscript (postprint) of the following publication:

Published Version:
Segatta F., Nenov A., Orlandi S., Arcioni A., Mukamel S., Garavelli M. (2020). Exploring the capabilities of optical pump X-ray probe NEXAFS spectroscopy to track photo-induced dynamics mediated by conical intersections. FARADAY DISCUSSIONS, 221, 245-264 [10.1039/c9fd00073a].

Availability:
This version is available at: https://hdl.handle.net/11585/732415 since: 2021-03-13

Published:
DOI: http://doi.org/10.1039/c9fd00073a

Terms of use:

Some rights reserved. The terms and conditions for the reuse of this version of the manuscript are specified in the publishing policy. For all terms of use and more information see the publisher's website.

This item was downloaded from IRIS Università di Bologna (https://cris.unibo.it/).
When citing, please refer to the published version.

(Article begins on next page)

12 October 2024

This is the final peer-reviewed accepted manuscript of:

Segatta, F.; Nenov, A.; Orlandi, S.; Arcioni, A.; Mukamel, S.; Garavelli, M. Exploring the Capabilities of Optical Pump X-Ray Probe NEXAFS Spectroscopy to Track Photo-Induced Dynamics Mediated by Conical Intersections. Faraday Discuss. 2019, 221 (0), 245–264.

The final published version is available online at: **https://doi.org/10.1039/C9FD00073A**

Terms of use:

Some rights reserved. The terms and conditions for the reuse of this version of the manuscript are specified in the publishing policy. For all terms of use and more information see the publisher's website.

This item was downloaded from IRIS Università di Bologna (https://cris.unibo.it/)

When citing, please refer to the published version.

Journal Name

ARTICLE TYPE

Exploring the capabilities of optical pump X-ray probe NEXAFS spectroscopy to track photo-induced dynamics mediated by conical intersections†

Francesco Segatta,*[a‡] Artur Nenov,*[a‡] Silvia Orlandi,[a] Alberto Arcioni,[a] Shaul Mukamel,[b] and Marco Garavelli*[a]

X-ray spectroscopy is gaining a growing interest in the scientific community, as it represents a versatile and powerful experimental toolbox for probing the dynamics of both core and valence electronic excitations, nuclear motions and material structure, with element and site specificity. Among the various X-ray based techniques, near-edge X-ray absorption fine structure (NEXAFS) spectroscopy, which interrogates the energy and probability of resonant core-to-valence transitions, has started to be applied to organic molecules: a recent UV-pump X-ray probe time resolved NEXAFS experiment [Wolf *et al., Nature Communication*, 2017, **8**, 1] has shown the capability of the technique to provide information about the ultrafast internal conversion between the bright $\pi\pi^*$ and the dark $n\pi^*$ electronic states of the nucleobase thymine. In the present contribution we introduce an accurate theoretical approach for the simulation of NEXAFS spectra of organic molecules, employing azobenzene as a testbed case. The electronic structure calculations, which provide both energy levels and transition probabilities of core-to-valence excitations, were here performed with a high level multiconfigurationl method, the restricted active space self consistent field (RASSCF/RASPT2). GS- and $n\pi^*$-NEXAFS spectra were obtained on the top of key molecular geometries (as the optimized *cis*, *trans* and conical intersection(s) structures) as well as along the fundamental isomerization coordinates (namely, symmetric and asymmetric bendings of the phenyl rings, and torsion around the central dihedral). We eventually characterize and explain the origin of the simulated signals, highlighting the specific signatures that make it possible to follow the excited state evolution from the $n\pi^*$ Franck Condon point, towards the conical intersection(s).

1 Introduction

Photoinduced nonadiabatic phenomena in molecules and supramolecular assemblies are ubiquitous. Conical Intersections (CI) open the door to ultrafast (sub-100-fs) nonradiative internal conversion between electronic states of the same spin multiplicity, controlling product yields and rates in virtually all photochemical and photophysical processes. Recent developments in multidimensional electronic spectroscopy, giving access to unprecedented short laser pulses with remarkable phase stability, have overcome the limitations of spectral congestion and low temporal resolution. This technical progress has provided the tools required to follow the ultrafast dynamics of molecular systems and holds the promise to reveal direct unambiguous fingerprints of the passage through a CI. The increasing complexity of the spectroscopic techniques gives rise to equally complex spectral signatures, whose direct interpretation is often hard or impossible. To disentangle all measured features and draw a detailed and reliable map of the energy transfer routes, it is therefore mandatory to support experimental measurements with theoretical models relying on a unified and fully integrated experimental-computational approach. Such an integrated approach has become paramount in the analysis and interpretation of transient optical spectroscopies, spanning the IR-VIS-UV spectral window. The development of X-ray free-electron laser facilities[1–3] paves the way to extend this approach to the rapidly growing field of novel multidimensional nonlinear spectroscopic techniques, ranging from X-ray Stimulated Raman[4] to time resolved X-ray diffrac-

[a] *Dipartimento di Chimica Industriale "Toso Montanari", Università degli studi di Bologna, Viale del Risorgimento 4, 40136 Bologna, Italy. E-mail: francesco.segatta2@unibo.it, artur.nenov@unibo.it,marco.garavelli@unibo.it*

[b] *Department of Chemistry, University of California, Irvine, CA 92697*

† Electronic Supplementary Information (ESI) available: [details of any supplementary information available should be included here]. See DOI: 10.1039/b000000x/

‡ These authors contributed equally to this work.

tion.[5]

X-ray spectroscopy provides a complementary tool for tracking of molecular excited state dynamics with respect to the more widely employed optical spectroscopy. Besides the improved temporal resolution which can be pushed down to the attosecond time scale, X-ray techniques are aspired because of their element- and site-selectivity: they allow to separate spectroscopically different elements even within the same molecule due to the strong difference in binding energy of core electrons ($\sim$100 eV difference for C, N and O). The subtle sensitivity of the binding energies to the composition of the immediate surrounding makes X-rays another promising tools for structural analysis[6] and for probing molecular dynamics.

Several X-ray techniques for tracking excited state molecular dynamics have emerged in the recent years.[7] In all such experiments, the photoactive molecule is initially excited by means of an optical pulse, populating a valence electronic state, and the excited state electronic structure is then probed by a delayed soft X-ray pulse. Near-edge X-ray absorption fine structure (NEXAFS) spectroscopy is used to probe resonant core-to-valence excitations.[8] In X-ray photoelectron emission (XPS), X-rays are used to eject a core electron from the molecule whose kinetic energy is recorder. Finally, X-ray emission spectroscopy (XES) studies the characteristic wavelengths of photons emitted by valence electrons when filling a previously generated core hole, a process known as Auger decay.[9]

The above techniques have been successfully applied in the transient X-ray spectroscopy of transition metal-based compounds.[9–11] More recently, applications to photo-energy and internal conversion in organic molecules have been reported.[12,13] In particular, the authors of Ref. 13 investigated the $\pi\pi^*$ to $n\pi^*$ internal conversion in thymine by means of time resolved NEXAFS. Wolf and co-workers exploited the fact that excitations from the thymine oxygen core can be promoted not only to unoccupied valence orbitals, but also to formerly occupied orbitals (of n and π character) in which the preceding optical excitation has created a hole. Moreover, the core-to-n transition was demonstrated to have high oscillator strength. Thus, the formation of the hole in the n orbital during $\pi\pi^*$ to $n\pi^*$ internal conversion was detected as a clear resonance below the K-edge in the absorption spectrum of the oxygen, thereby demonstrating the sensitivity of the technique to capture the ultrafast $\pi\pi^*$ to $n\pi^*$ internal conversion (on a sub-ps time scale).

In this contribution we extend the idea and explore, by means of theoretical simulations, the sensitivity of optical pump near-edge X-ray probe spectroscopy to photoinduced excited state dynamics in conjugated organic molecules containing heteroatoms with electron lone pairs. By means of the multiconfigurational restricited active space self consistent field (RASSCF) approach[14] corrected by second order perturbation (RASPT2)[15,16] we simulate NEXAFS spectra of azobenzene probing the ground state (GS) and the $n\pi^*$ excited state at representative molecular geometries. Recently, Ehlert *et al.* published a theoretical study of the GS-, $n\pi^*$- and the $\pi\pi^*$-NEXAFS spectra of *trans*- and *cis*-azobenzene performed within the framework of density functional theory (DFT).[17] Our study extends beyond the Franck-Condon (FC) points and covers the entire isomerization pathway connecting the *trans*- and the *cis*-forms. Furthrmore, we derive a simple orbital-based model which successfully rationalizes the observed spectral shifts and line shapes.

Our simulations reveal characteristic signal trends along key modes involved in the isomerization of azobenzene, i.e. torsion and bending. We note, however, that the documented trends are generally valid for any *cis-trans* isomerization reaction. While in conventional (optical) spectroscopy techniques the evidence of passage through a crossing region is merely extrapolated (due to extremely red-shifted signals and cancellation of their oscillator strength[18]), here we demonstrate a clear indication of a system evolution towards and through the CI which can be directly observed with X-ray techniques provided they have the required temporal resolution.

Finally, we discuss the transferability of the findings to other systems for which the here observed NEXAFS features can be exploited to track their photoinduced dynamics and to pinpoint in time the passage through the CI. In summary, we expect organic molecules containing hereroatoms with electron lone pairs (like nucleobases, amino acids, and more general azoswitches) and exhibiting a ballistic motion of the excited state wave packet towards the CI, to be good candidates for a clean time resolved mapping of the excited state potential energy surface with the already available X-ray techniques.

2 Computational Details

Core excitations in molecular systems absorb above several hundreds of eV and are thus preceded by a vast number of valence states. Therefore, a strategy is required to target specifically desired core excitations. The restricted active space self consistent field (RASSCF) approach[14] from the family of multi-configuration wavefunction based methods offers a neat way to cope with this issue. In a RASSCF calculation the active space, i.e. the list of orbitals and electrons of paramount importance for describing the electronic structure of the system, is divided into subspaces: RAS1 with an upper limit of holes; RAS2 where all permutations of electrons within the orbitals are considered; RAS3 with a maximal number of simultaneously excited electrons. In this regard, RASSCF offers a higher flexibility with respect to the more commonly used complete active space approach (CASSCF) which does not distinguish between subspaces,[19,20] thus effectively removing "dead wood" from the list of configuration state functions (CSF's) without sacrificing accuracy. The missing (dynamical) correlation can be added on top of a RASSCF calculation through second-order perturbation (RASPT2).[15,16,21]

A common strategy to treat core-valence excitations within the RASSCF/RASPT2 framework is to place the core orbital(s) in RAS3 and use an upper limit of $n-1$ electrons into this subspace with n being the total number of electrons in the fully occupied core orbital(s). Thereby, the list of CSF's is forced to include only core-hole configurations. This strategy has been applied to compute near edge X-ray spectroscopy of metal complexes[22,23] as well as X-Ray Raman of organic compounds.[24] A considerable drawback of this approach is that the core-valence transition dipole moments are not straightforwardly accessible due to

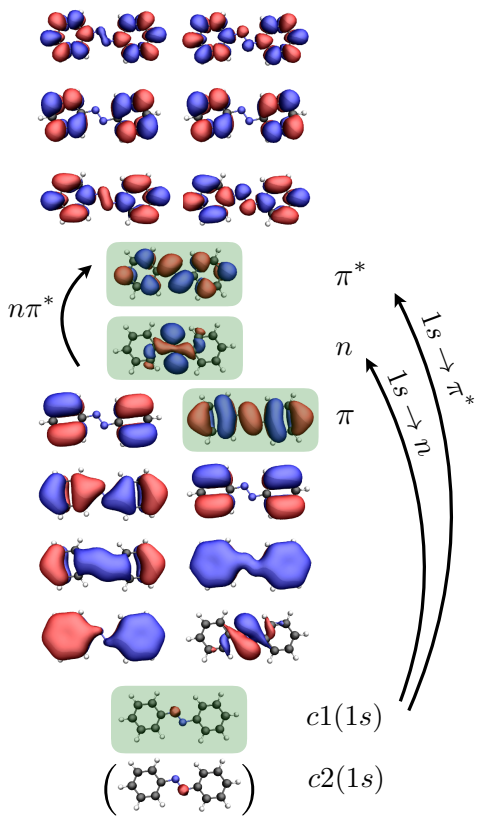

Fig. 1 Active space (in order of the orbital occupation) of the SA2-RASSCF(1,1|18,9|4,7) *trans*-azobenzene valence states computation and diagram of the transitions relevant to this work. Key orbitals are highlighted in green colored boxes. If not otherwise specified, the nitrogen lone pair n and the π^* orbital refer to, respectively, the highest occupied and the lowest unoccupied orbitals. The two core orbitals are denoted with the labels $c1$ and $c2$.

the fact that valence and core-hole states need to be computed with different RAS3 limits for maximal occupation (n for valence states, $n-1$ for core-hole states).

Here we utilize a novel projection technique recently implemented in OpenMolcas,[25] called *highly excited states* (HEXS) which sets to zero the CI coefficients of all CSF's with the maximum occupation from a given subspace, thus effectively projecting them out of the wavefunction.[26] The HEXS approach allows to model the transition dipole moments of the core-excited states. Furthermore, the HEXS technique allows to handle mixed core-excitations, e.g. by placing different core orbitals in RAS1 and RAS2 and applying the projector operator to both, and can be straightforwardly extended to multiple core excitations.[26] This offers intriguing possibilities in combination with the generalized version of the RASSCF technique, known as GASSCF,[27,28] which removes the restriction of working with only three subspaces. Applications of the HEXS technique can be found in Ref. 22,29,30.

In the following we outline the protocol for computing the nitrogen near edge X-ray spectra in azobenzene:

1. a Hartree-Fock calculation is performed which is used to construct the active space; due to the symmetry of azobenzene the canonical nitrogen core orbitals are delocalized; in order to calculate contributions from individual cores, core-localized orbitals are obtained by linear combination;

2. the active space is constructed as follows (see Figure 1):

   - RAS1: one core orbital is placed herein and kept frozen to avoid orbital rotation (using the SUPSYM keyword); the upper limit of holes was set to 1;
   - RAS2: all occupied valence π-type orbitals were placed herein;
   - RAS3: all virtual valence π^*-type orbitals were placed herein and an upper limit of 4 excitations was set;

   In the following we designate the active space as RAS$(1,1|18,9|4,7)$, where the first pair of indices denote the upper limit of holes and the number orbitals in RAS1, the second pair the number of electrons and orbitals in RAS2, the third pair the upper limit of excitations and the number of orbitals in RAS3;

3. RASSCF calculations were performed separately:

   - for the valence states, where up to two states (ground state (GS) and $n\pi^*$ states), were included in the state-averaging, i.e. SA-2-RASSCF$(1,1|18,9|4,7)$. In case of configuration mixing between the first two roots (e.g. encountered for structures close to 90° torsion) state-averaging was performed over the first three roots;
   - for each of the two nitrogen core-orbitals, where the HEXS keyword was utilized to force the creation of the core hole, and up to 15 states were included in the state-averaging, i.e. SA-15-core-RASSCF$(1,1|18,9|4,7)$; in structures exhibiting symmetry with respect to the nitrogen core-orbitals it is sufficient to perform the computations accounting for only one of the two cores.

4. unless specified otherwise in the text single state (SS)-RASPT2 was performed on top of each RASSCF calculation to account for the dynamical correlation; calculations have been performed setting the ionization-potential electron-affinity shift[31] of 0.0 Hartree; to reduce problems with intruder states an imaginary shift[32] of 0.3 Hartree has been applied;

5. transition dipole moments between the sets of valence and core-hole states were computed through the RAS state interaction (SI) routine;

6. the transition energies ω and the transition dipole moments TDM were used to simulate near edge X-ray absorption spectra with the ground and first excited state ($n\pi^*$) as reference, denoted GS-NEXAFS and $n\pi^*$-NEXAFS, respectively. The stick spectrum was dressed by a gaussian broadening, given by the equation

$$NEXAFS(\omega) = \frac{1}{\sigma\sqrt{2\pi}} \sum_i |TMD_{S_x \rightarrow i}|^2 \exp\left[\frac{-(\omega - \omega_{S_x \rightarrow i})^2}{2\sigma^2}\right] \quad (1)$$

   where S_x represents either the GS or the $n\pi^*$ state, the sum runs over the core-hole excited state and a standard deviation of 0.4

eV (corresponding to a full-width-at-half-maximum broadening of ∼0.9 eV) was used.

Scalar relativistic effects have been included by using a second-order Douglas-Kroll-Hess Hamiltonian in combination with a relativistic atomic natural orbital basis set, ANO-RCC.[33] A triple-ζ basis function set augmented with two sets of d-functions was used for carbons and nitrogens, whereas an additional set of f-functions was used to improve the description of nitrogen, thus giving rise to ANO-RCC: C[4s3p2d1f], C[4s3p2d], H[2s1p]. A density-fitting approximation of the electron repulsion integrals has been used, knows as Cholesky decomposition.[34]

Calculations were performed on a variety of azobenzene geometries:

- the *cis*- and *trans*- GS minima;
- varying the three degrees of freedom of paramount importance for the *cis*- to *trans*- photoisomerization: torsion (CNNC), symmetric and asymmetric bending angles CNN/NNC:
  - CNNC=140° (CNN/NNC=126°), CNNC= 120° (CNN/NNC=124°) and CNNC=100° (CNN/NNC=122°);
  - CNN/NNC=114° (CNNC=180°), CNN/NNC=122° (CNNC=180°) and CNN/NNC=126° (CNNC=170°).
  - CNN=112°/NNC=116°, CNN=112°/NNC=124° and CNN=112°/NNC=142°, for a fixed value of CNNC=180°.
- the conical intersections (CIs) between the ground and $n\pi^*$ state: the minimum energy CI, characterized by a central torsion CNNC=90° and asymmetric bending angles CNN/NNC=116°/146°, and a planar (CNNC=180°) CI, characterized by large bending angles CNN/NNC=150°/150°;
- along the the minimum energy path which connects the *trans*-azobenzene Franck-Condon point on the $n\pi^*$ state with the lowest $n\pi^*$/GS conical intersection.

The minima were optimized at the MP2/ANO-L-VDZP level, the mimimum energy CI at the MS-2-RASPT2/SA-2-RASSCF$(4,9|0,0|4,7)$ level (employing PT2 numerical gradients). The key molecular modes were studied through rigid scans. The minimum energy path was taken from a recently performed three-dimensional rigid scan along the key modes performed by some of the present authors.[35] All calculations were performed in gas-phase with the OpenMolcas suite.[25]

3 Results

In this section we show our results for GS- and $n\pi^*$-NEXAFS spectra computed at the previously listed molecular geometries, and introduce a model capable of explaining the simulated data (summarized in Figure 4). NEXAFS spectra are characterized by isolated features from resonant states below the core ionization edge of an element. These features are originated by transitions from the element's core orbital to unoccupied valence orbitals, e.g. a π^* orbital. The intensity of such core-to-valence transitions is determined by the spacial overlap between the confined core and the valence orbital.[8,36]

In NEXAFS spectra from excited states, additional features may appear. In a single electron Hartree-Fock picture, an excited state can be described as an electron-hole pair in a formerly occupied and an unoccupied molecular orbitals: azobenzene $\pi\pi^*$ state is *mainly* described by a removal of one electron from the highest occupied molecular orbital, which is then placed in the lowest unoccupied molecular orbitals, both with π symmetry; azobenzene $n\pi^*$ state is instead characterized by the filling of the same π^* orbital, with an electron coming from the nitrogen lone pairs. The creation of such a hole in a formerly occupied valence orbitals, enables an additional NEXAFS resonance to be visualized when probing the (VIS/UV) excited system with an X-ray pulse.

The fact that the absorption cross-section of the various core-level transitions mainly depend on the spacial overlap between the starting and arrival orbitals, makes it clear why the $1s \rightarrow n$ transition from the strongly localized heteroatom $1s$ core to the electron hole of the $n\pi^*$ state should appear brighter than the $1s \rightarrow \pi$ transition from the same core to the more delocalized π orbital of a $\pi\pi^*$ state. This idea was exploited by Wolf *et. al.*[13] to show the internal conversion rate between the $\pi\pi^*$ state (characterized by a weak $1s \rightarrow \pi$ transition) to $n\pi^*$ state (with a much stronger $1s \rightarrow n$ transition), performing time resolved NEXAFS experiments at the thymine oxygen K-edge.

In what follows we will focus on nitrogen spectral signatures originated by the intense $1s \rightarrow \pi^*$ and $1s \rightarrow n$ transitions. These fall approximately in the region between 395 and 400 eV. Core transitions to higher π^* orbitals and virtual orbitals outside the active space are blue-shifted with respect to this window. Since these are generally a large number of low-intensity, overlapping signals, it is more difficult to extract information in that region of the spectrum. This was the reason, together with a reduced computational cost, why we limit ourselves to the computation of 15 core-level excitations in the active space of Figure 1, and focus our analysis on the clean and informative signals of the 395-400 eV window.

3.1 NEXAFS on *cis*- and *trans*-azobenzene

GS-NEXAFS and $n\pi^*$-NEXAFS spectra computed at the optimized GS minima of *cis*- and *trans*-azobenzene are shown in Figure 2. The gross features are here summarized: the presence of the intense $1s \rightarrow \pi^*$ transition in both the GS- and $n\pi^*$-NEXAFS spectra between 398-399 eV, and the appearance of the additional, red-shifted, $1s \rightarrow n$ transition uniquely in the $n\pi^*$-NEXAFS spectrum around 396 eV. The weaker contributions observed above 400 eV are assigned to transitions into higher π^* orbitals. The weak intensity is attributed to the fact that the higher lying π^* orbitals are mainly localized on the phenyl-moieties effectively decreasing the spatial overlap. A more detailed analysis of the transitions is reported in Table 1. Interestingly enough, from a qualitative point of view, the NEXAFS spectra for both geometries exhibit similar features in terms of peak positions, nature of the transition and intensity with spectral shifts of about 0.5 eV. Notably, the gap between the $1s \rightarrow n$ and $1s \rightarrow \pi^*$ bands is larger by ca. 1 eV in *trans*-azobenzene with respect to the *cis*-form. We also note that the contributions from both nitrogens (c1 and c2) to the NAXAFS

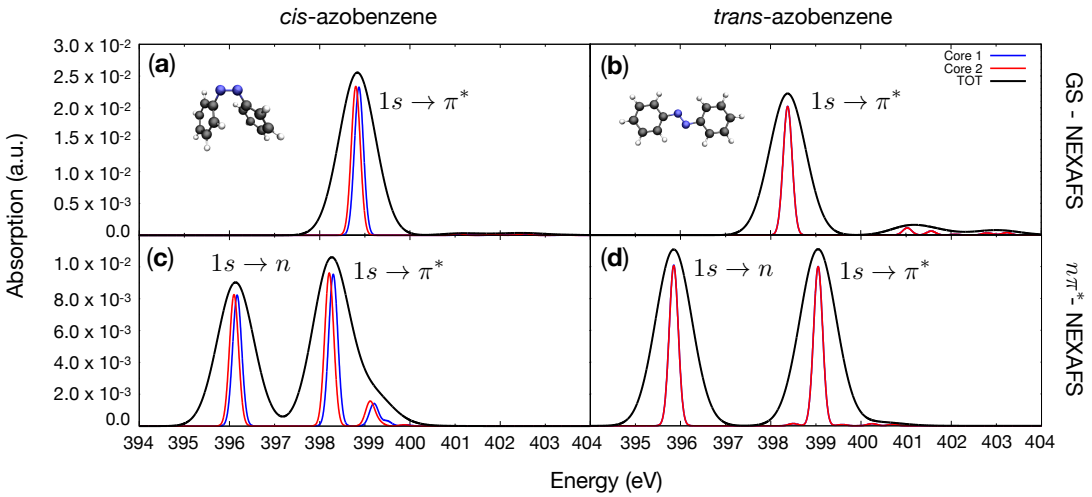

Fig. 2 NEXAFS spectra for *cis*-azobenzene (a,c) and *trans*-azobenzene (b,d). Color spectra are obtained with a broadening of 0.1 eV and correspond to exciting cores c1 (blue) and c2 (red, see Figure 1 for notation). The black spectrum represents the sum of the individual core spectra with a broadening of 0.4 eV. The molecular structure is also reported in the inset of (a) and (b). (a) and (b) show GS-NEXAFS, (c) and (d) show $n\pi^*$-NEXAFS of both species.

	Peak label	Main Config.	Weight	Energy (PT2)	$\lvert TDM \rvert^2$	Peak label	Main Config.	weight	Energy (PT2)	$\lvert TDM \rvert^2$
		cis-azo					*trans*-azo			
GS - NEXAFS	-	$1s^{[1]}n^{[2]}\pi^{*[1]}$	0.90	398.9	5.82×10^{-3}	-	$1s^{[1]}n^{[2]}\pi^{*[1]}$	0.89	398.4	5.07×10^{-3}
$n\pi^*$ - NEXAFS	-	$1s^{[1]}n^{[2]}\pi^{*[1]}$	0.90	396.2[a]	2.07×10^{-3}	-	$1s^{[1]}n^{[2]}\pi^{*[1]}$	0.89	395.9	2.53×10^{-3}
	-	$1s^{[1]}n^{[1]}\pi^{*[2]}$	0.67	398.3[a]	2.39×10^{-3}	-	$1s^{[1]}n^{[1]}\pi^{*[2]}$	0.90	399.1	2.46×10^{-3}
	-	$1s^{[1]}n^{[1]}\pi^{*[2]}$	0.36	399.2[a]	3.48×10^{-4}					

Table 1 Report of the properties of the main peaks observed in Figures 2: configurations with the highest weight, weight, RASPT2 energies (in eV), and the module squared of the transition dipole moment (in a.u.^{2}). Configurations are labeled by occupation number of the three orbitals 1s, n, and π^*.
[a] These values are computed at the MS-RASPT2 level.

spectra are identical (blue and red bands in Figure 2). This is related to the symmetry of these molecular structures, which makes the two core indistinguishable by definition. The slight splitting of the $1s \rightarrow \pi^*$ band observed in the *cis* NEXAFS spectra is an artifact of a strong state mixing of energetically close lying roots at the RASSCF level (see Table 1) leading to a pronounced artificial peak splitting. This mixing is largely corrected at the multi-state RASPT2 level, the results of which are plotted in Figure 2.

These FC spectra can be compared to those reported recently by Ehlert and co-workers,[17] computed within the density functional theory framework, in combination with transition potential and ΔSCF methodology (TDDFT/ΔSCF). Focusing on the 395-400 eV spectral region, one observes that the GS-NEXAFS is characterized by the same intense $1s \rightarrow \pi^*$ transition blue-shifted by ca. 1.5 eV with respect to our calculations. Regarding the $n\pi^*$-NEXAFS Ehlert and coworkers successfully predict the appearance of a red-shifted peak, associated with the $1s \rightarrow n$ transition (again, slightly blue-shfited with respect to our results). Notably, the $n\pi^*$-NEXAFS of Ref. 17 do not show the peak related to the $1s \rightarrow \pi^*$ transition, which is instead clearly visible in our simulations. The reason for this discrepancy could be found in the fact that TDDFT is essentially blind to doubly excited states, such as the one generated out of the $n\pi^*$ state through the $1s \rightarrow \pi^*$ excitation. In multi-configuration wave function methods, instead, single and many electron excitations are described at equal footing.

3.2 NEXAFS along key molecular modes

It has been demonstrated previously that the *cis-trans* isomerization in azobenzene can be described in terms of few important coordinates, namely: the CNN/NNC bendings and the torsion around the central CNNC dihedral.[35,37,38] In Figure 3 we show the effect of the motion along 1) symmetric CNN/NNC bending, 2) CNNC torsion and 3) asymmetric CNN/NNC bendings on the simulated GS- and $n\pi^*$-NEXAFS spectra. In particular, we observe that:

1. Symmetry-conserving variation of the CNN/NNC bending values does not affect the $1s \rightarrow \pi^*$ transition in both GS- and $n\pi^*$-NEXAFS. At the same time, the motion along this coordinate produces a clear blue-shift of the $1s \rightarrow n$ transition in the $n\pi^*$-NEXAFS spectrum (bottom part of Figure 3).

2. Vice versa, $1s \rightarrow n$ transition is insensitive to motion along the CNNC torsion, which instead causes the $1s \rightarrow \pi^*$ peak to red-shift in both NEXAFS spectra from the FC geometries (CNNC values 0°and 180°) towards the 90° twisted geometry (central part of Figure 3).

3. Asymmetric variation of the CNN/NNC bending angles intro-

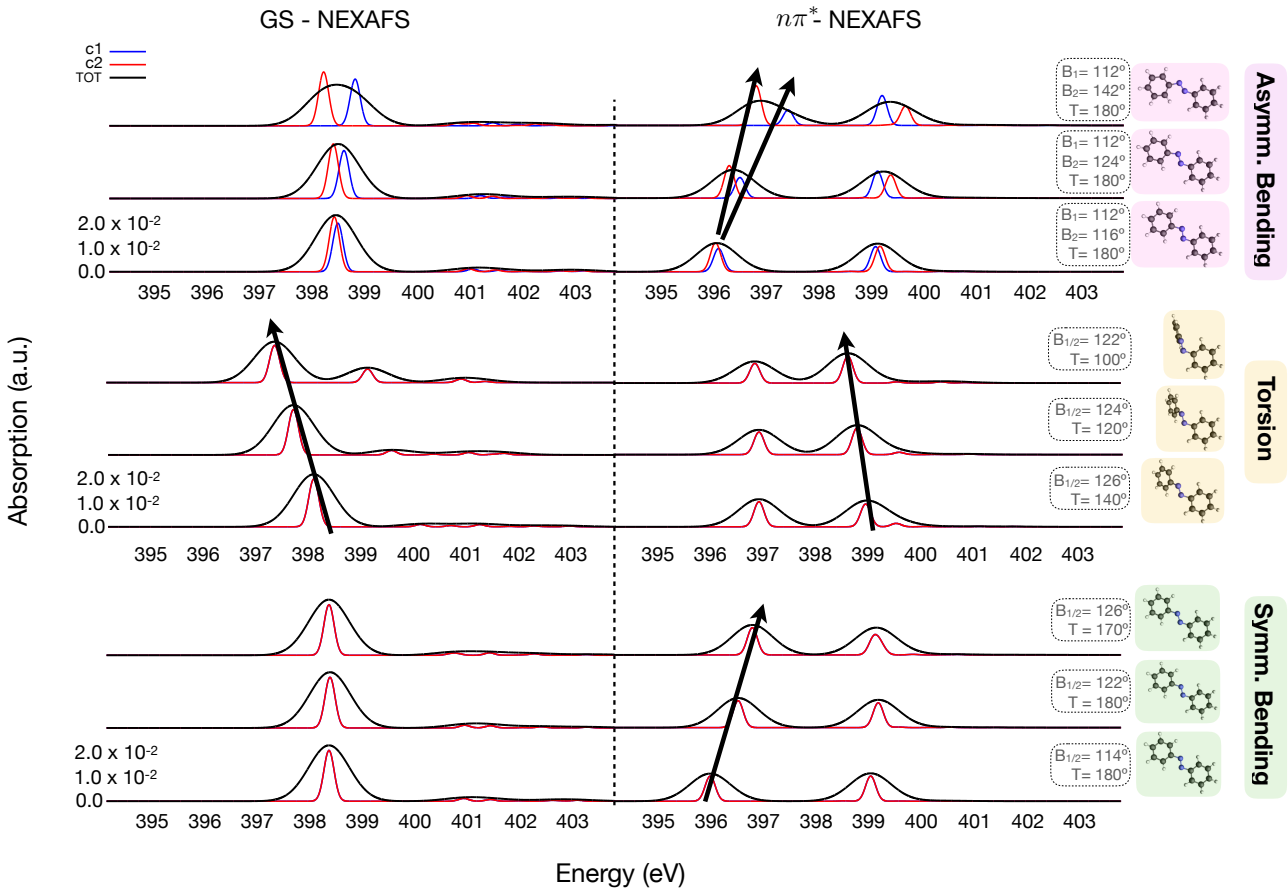

Fig. 3 Impact of geometrical distortions along key molecular modes on GS- and $n\pi^*$-NEXAFS spectra, namely symmetric CNN/NNC bending (bottom panel), CNNC torsion (middle panel) and asymmetric CNN/NNC bending (top panel). The spectral shifts of the peaks is highlighted by black arrows. Molecular structures with the corresponding values for torsion and bending angles are also shown (labels B_1 and B_2 refer to CNN and NNC bending respectively, while T stands for the CNNC torsion).

duces a novel feature, namely, it breaks the symmetry thus making the two cores non-equivalent. As a consequence, core-specific signals appear which affect all signals (top part of Figure 3). As expected, variation of the CNN/NNC bending values blue-shifts of the $1s \rightarrow n$ transitions, however, the c1 and c2 contributions are affected to a different extent, giving rise to a pronounced broadening of the peak when realistic peak broadening is applied. Similar peak broadening is observed also for the $1s \rightarrow \pi^*$ transitions. Interestingly enough, the c1 signals always appear en-framed by c2 signals.

3.3 Molecular orbital based rationalization of the observed trends

In order to rationalize the observed signal trends along the specific modes, we build a simple model which involves only a limited number of orbitals, namely: the two nitrogen $1s$ core orbitals c1 and c2, their lone pair n (being the highest occupied molecular orbital), the π and the π^* (which is the lowest unoccupied orbital) highlighted by the color boxes in Figure 1. The model is reported in Figure 4.

The model assumes that the energies of the core orbitals are not affected by the geometrical deformations as they are localized at the nitrogens. The spectral shifts observed in the NEXAFS spectra are rather understood as a function of the valence orbital energies exhibit mode-specific dependence. For example, the red-shift of the $1s \rightarrow \pi^*$ transition in both the GS- and $n\pi^*$-NEXAFS spectra along the torsional coordinate connecting the FC points of *cis*- and *trans*-azobenzene with the 90° twisted geometry (central part of Figure 3) is a consequence of the associated stabilization of the π^* orbital due to the decreasing anti-bonding character. Similarly, symmetry-conserving CNN/NNC bending deformations with respect to the $n\pi^*$ equilibrium value of 126° increase the energy of the n orbital due to increasing Coulomb repulsion of the lone pair electrons and the rest of the system. This effectively increases the core-n orbital band gap and induces a blue-shift of the core-n transition in the $n\pi^*$-NEXAFS spectrum.

In order to explain the band splitting in case of asymmetric deformations it is necessary to have a more in-depth look at the electronic structure of the core-hole states. The valence π orbitals of core-saturated azobenzene are delocalized over the entire molecule body giving rise to a strongly conjugated π-system, whereas the lone pair is localized on the central fragment. The removal of one electron from the $1s$ orbital of nitrogen upon core-excitation decreases dramatically the electronic shielding effect of the nuclear positive charge. As a consequence the elec-

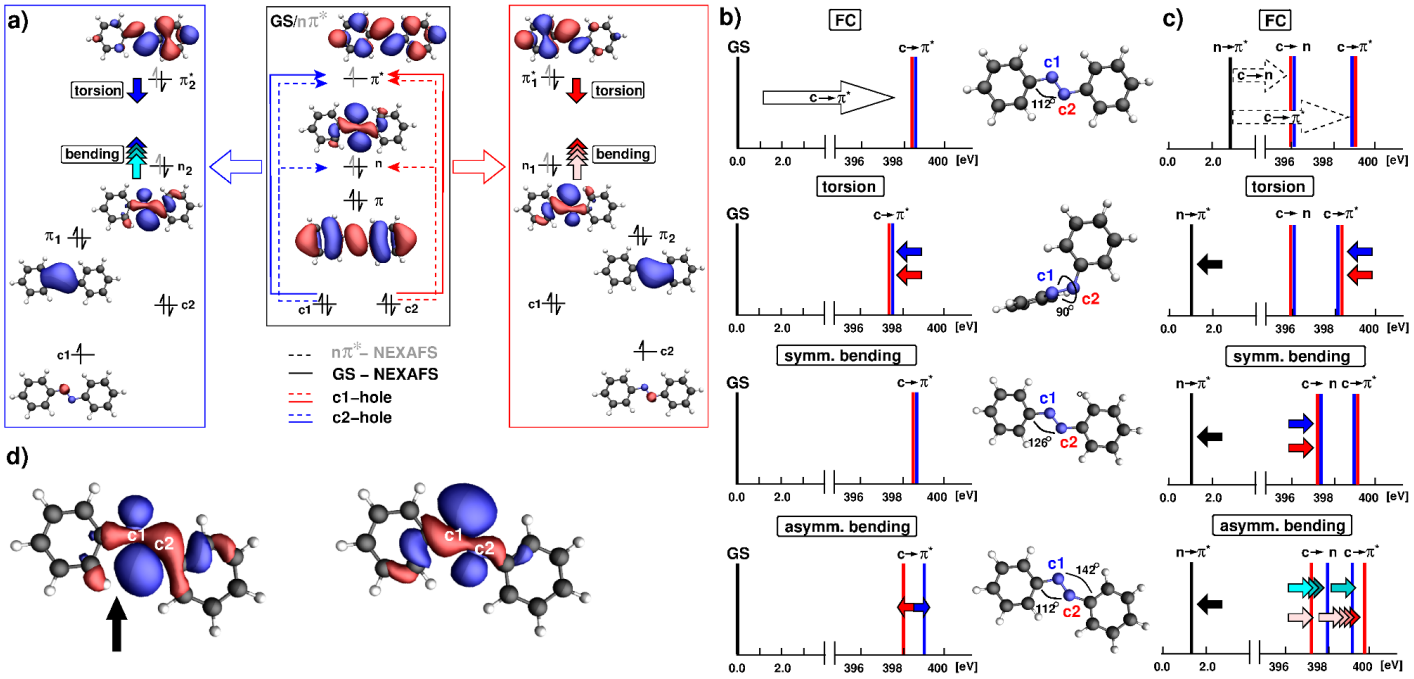

Fig. 4 Molecular orbital model used to rationalize the observed trends in the simulated NEXAFS spectra. (a) The central box shows the valence orbitals π, π^* and the lone pair n and highlights possible core-valence transitions from either c1 or c2 (in blue and red) out of the GS and out of the $n\pi^*$ state, giving rise to the GS- and $n\pi^*$-NEXAFS spectra, respectively. Side boxes show the localization effect on the valence orbitals which accompanies a core-excitation. (b,c) Schematic representation of the impact of geometrical distortions along key molecular modes on GS-NEXAFS (b) and on the $n\pi^*$-NEXAFS (c) with respect to the spectra in the Franck-Condon region (first row). A description of the model is outlined in Section 3.2. (d) Localization pattern of the lone pairs upon core-excitation of c1 (left) and c2 (right) in an asymmetrically distorted *trans*-azobenzene (CNN/NNC=112°/142°).

tronegativity of the core-excited nitrogen increases and it withdraws electron density from the neighboring atoms. Mulliken charge analysis reveals that core-excited nitrogen accumulates nearly a unit negative charge, even if it has a core-hole. The enhanced electron-withdrawing effect of the core-excited center translates into lowering the energy of its atomic orbitals. For example, Figure 4,a) shows how upon core-excitation the nitrogen p-type orbital decouples from the aromatic system thus breaking the conjugation, and localizes on the core-excited center. The frontier lone pair, instead, localizes on the opposite center. In symmetric geometries one can expect to encounter symmetry-preserving orbitals due to the equivalence of the core-excited centers. However, in asymmetric geometries the localization is likely to dominate. The localization of the frontier lone pair during core-excitation in asymmetrically bent azobenzene leads to a non-uniform blue-shift of the $1s \rightarrow n$ transitions (Figure 4,c) bottom panel) as in one of the two localized lone pairs the Coulomb repulsion with the surrounding is stronger. This effect is demonstrated in Figure 4,d) for an azobenzene having a pair of bending angles CNN/NNC=112°/143°. As evident, an electron pair in the frontier n orbital of the c1-hole system, localized predominantly on c2, is subjected to a strong repulsion with the neighbouring phenyl hydrogen. The repulsion is less pronounced for the frontier n orbital of the c2-hole system. Consequently, localizing the lone pair in the c1-hole (blue component in the $c \rightarrow \pi^*$ and $c \rightarrow n$ dual peak in Figure 4,b)-c) bottom panel) requires more energy with respect to the c2-hole. The stronger repulsion to which the lone pair of the c1-hole is subjected makes a subsequent $n \rightarrow \pi^*$ excitation energetically more favorable. This explains the inverted order of the blue and red components in the $1s \rightarrow \pi*$ band of the $n\pi^*$-NEXAFS spectrum.

The introduced model is therefore capable of explaining the observed behaviours in the simulated spectra, in terms of stabilization and destabilization of the frontier orbitals π^* and n, respectively, accompanied by localization in case of symmetry breaking.

3.4 NEXAFS signals at the conical intersections

In Figure 5 we report NEXAFS spectra for two representative CIs between the ground and $n\pi^*$ states: the asymmetrically bent minimum energy CI, characterized by a central torsion CNNC=95° and a bending angle pair CNN/NNC=116°/146°(Figure 5,a) and c)) and a symmetry-conserving planar (CNNC=180°) CI, characterized by large bending angles CNN/NNC=150/150°(Figure 5,b) and d)). We avoid the notation GS and $n\pi^*$ when dealing with CIs and use, instead, the notation *closed-shell* and *open-shell* as both configurations are virtually degenerate at the crossing and change energetic order along various degrees of freedom.

We note the pronounced difference between the closed-shell NEXAFS spectra for both species (Figure 5,a) and b)). The spectrum of the asymmetric CI shows two clear peaks, both associated with a $1s \rightarrow \pi^*$ transition, either from c1 or c2. As elucidated in the previous section, the non-equivalence of the two cores induces a splitting of the $1s \rightarrow \pi^*$ band which for large asymmetric deformations could reach values as large as 1.5 eV, well beyond the

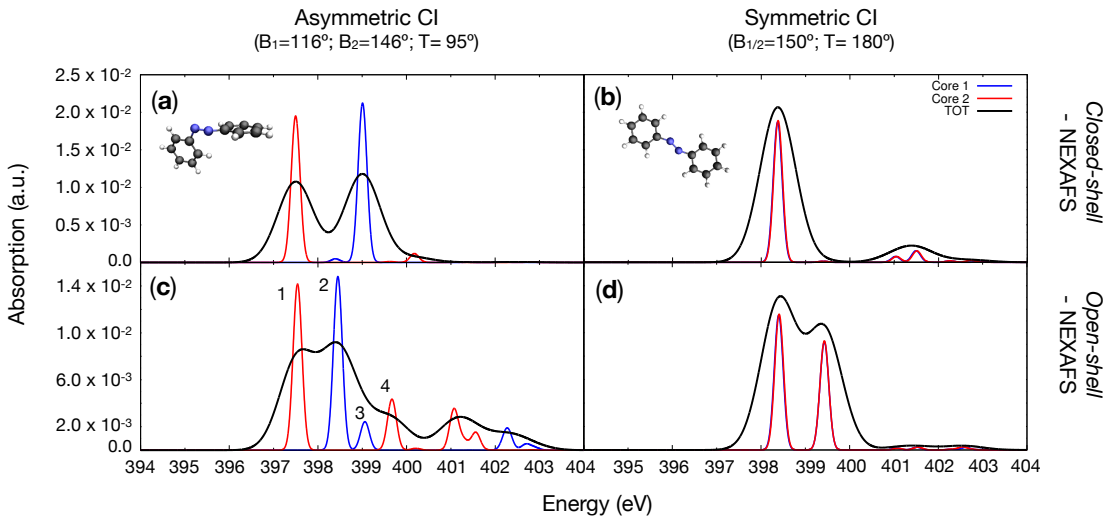

Fig. 5 GS- and $n\pi^*$NEXAFS spectra of the symmetry-breaking minimum energy CI with central torsion CNNC=90°(a,c) and of a symmetry-conserving CI accessible from the *trans*-side characterized by large CNN/NNC bending value of 150° (b,d). The molecular structure is also reported in the inset of (a) and (b). Color spectra are obtained with a broadening of 0.1 eV and correspond to exciting cores c1 (blue) and c2 (red, see Figure 1 for notation). The black spectrum represents the sum of the individual core spectra with a broadening of 0.4 eV. (a) and (b) show *closed-shell*-NEXAFS, (c) and (d) show *open-shell*-NEXAFS of both species.

	Peak label[a]	Main Config.	Weight	Energy (PT2)	$\lvert TDM \rvert^2$	Peak label	Main Config.	weight	Energy (PT2)	$\lvert TDM \rvert^2$
		Asymmetric CI (c1)					Asymmetric CI (c2)			
GS - NEXAFS	-	$1s^{[1]}n^{[2]}\pi^{*[1]}$	0.78	399.0	5.32×10^{-3}	-	$1s^{[1]}n^{[2]}\pi^{*[1]}$	0.89	397.5	4.89×10^{-3}
$n\pi^*$ - NEXAFS	2	$1s^{[1]}n^{[2]}\pi^{*[1]}$	0.83	398.5	3.71×10^{-3}	1	$1s^{[1]}n^{[2]}\pi^{*[1]}$	0.89	397.5	3.55×10^{-3}
	3	$1s^{[1]}n^{[1]}\pi^{*[2]}$	0.78	399.1	6.09×10^{-4}	4	$1s^{[1]}n^{[1]}\pi^{*[2]}$	0.78	399.7	1.09×10^{-3}
		Symmetric CI								
GS - NEXAFS	-	$1s^{[1]}n^{[2]}\pi^{*[1]}$	0.89	398.4	4.68×10^{-3}					
$n\pi^*$ - NEXAFS	-	$1s^{[1]}n^{[2]}\pi^{*[1]}$	0.89	398.4	2.88×10^{-3}					
	-	$1s^{[1]}n^{[1]}\pi^{*[2]}$	0.90	399.4	2.31×10^{-3}					

Table 2 Report of the properties of the main peaks observed in Figures 5: configurations with the highest weight, weight, RASPT2 energies (in eV), and the module squared of the transition dipole moment (in a.u.^{2}). Configurations are labeled by occupation number of the three orbitals 1s, n, and π^*.
[a] The peak labels refer to those of Figure 5.

FWHM width of the peak. The closed-shell spectrum of the symmetric CI is characterized by a single peak which exhibits virtually no shift with respect to the GS-NEXAFS at the FC point. This observation is in agreement with the notion that the GS/closed-shell NEXAFS spectrum does not change along the bending degree of freedom (bottom part of Figure 3).

The realistically broadened open-shell NEXAFS spectra of both species have similar line shapes (Figure 5,c) and d)), characterized by a single broad band with fine structure. However, the underlying transitions are rather different. The main contribution to the spectrum of the asymmetric CI arises from the splitting of the $1s \rightarrow n$ transitions, whereas the $1s \rightarrow \pi^*$ signals are less intense. Remarkably, the repulsion of the doubly occupied lone pair in the c1-hole state (peak 2 in Figure 5,c)) becomes so large due to the strong asymmetric deformation (Figure 4,d)) that promoting an electron out of the n orbital into the π^* is done at almost no cost (peak 3 in Figure 5(c) blue-shifted by 0.5 eV). The broadening of the open-shell spectrum of the symmetric CI is the result of the strong destabilization of the n orbital along the bending coordinate by about 2.5 eV with respect to the FC spectrum of the *trans*-form (Figure 2,d)) which causes the blue-shift of the $1s \rightarrow n$ transition from 396 eV to 398.5 eV, in agreement with our model (Figure 4,c)).

On the basis of the previous analysis we can conclude that conical intersections exhibit a characteristic spectral fingerprint which may be used to track a wave packet evolving on the $n\pi^*$ state potential energy surface when it approaches the crossing seam. This signature is a single broad band spanning the entire 397-400 eV spectral window and exhibiting a fine structure which originates either from the merging of the $1s \rightarrow n$ and $1s \rightarrow \pi^*$ bands, clearly separated at in the FC region, into a single broad peak in the open-shell NEXAFS (symmetric CI), or by the core splitting of the $1s \rightarrow n$ transition, with minor contributions from the $1s \rightarrow \pi^*$ transitions (asymmetric CI). The asymmetric CI seam exhibits another characteristic signature, a double-peak structure of its closed-shell spectrum, otherwise dominated by a single peak.

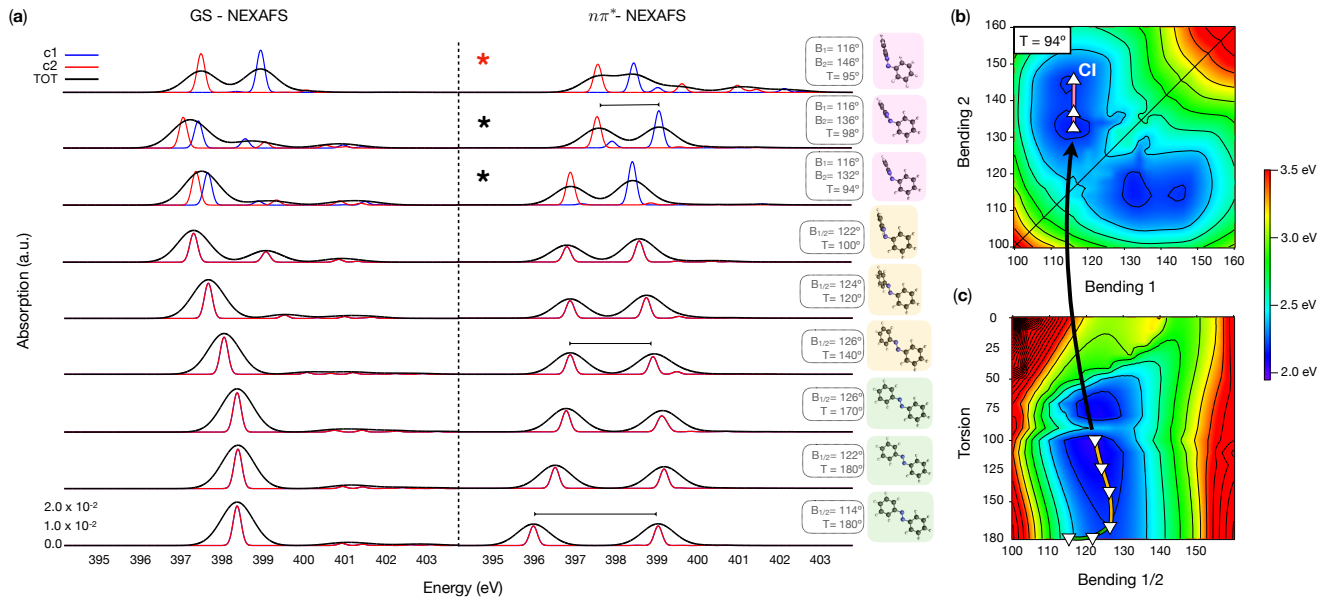

Fig. 6 (a) GS- and $n\pi^*$-NEXAFS spectra along the minimum energy path (MEP) on the potential energy surface of $n\pi^*$ state from the Franck-Condon point of *trans*-azobenzene towards the asymmetric CI. The path itself is visualized as heat maps in the coordinate subspace of CNNC torsion and symmetric CNN/NNC bending (b) and in the subspace of both bendings at a fixed torsion T=94° (c). The maps are plotted using MS-2-RASPT2/ SA-2-RASSCF$(4,9|0,0|4,7)$ $n\pi^*$ energies from a rigid scan with the energy of the GS *trans*-minimum set as zero point reference.[35] The first six spectra (from the bottom) and the last one, have been already reported in Figure 3 and 5, respectively.

3.5 Minimum energy path

After discussing the dependence of the NEXAFS spectra on the geometrical deformations along key molecular modes and after becoming acquainted with the characteristic spectral features of the crossing region we are now in position to apply optical-pump NEXAFS-probe spectroscopy to track the photo-induced *tans*- to *cis*- isomerization. A comprehensive non-adiabatic dynamics is out of the scope of the present study which focuses only on the spectral dynamics along the MEP connecting the FC region of the *trans*- form with the minimum energy CI. Figure 6(b,c) show the excited state profiles in the coordinate space of torsion and symmetric bending angles (c), as well as in the coordinate space of both bending angles (b) together with the MEP (the thick colored line which connects the points). Figure 6(a) reports a sequence of GS- and $n\pi^*$-NEXAFS spectra simulated along few selected structures along the MEP. Upon photo-excitation azobenzene exhibits gradient directed along the symmetric bending coordinate which widens the CNN/NNC angles, a deformation associated with a blue-shift of the $1s \rightarrow n$ peak in the $n\pi^*$ spectrum. Molecular dynamics simulations have revealed that the initial motion along the symmetric bending coordinate explores a range of bending angle values of around ∼30/40°and remains coherent for several oscillation periods.[35] This would translate into an oscillatory $1s \rightarrow n$ spectral dynamics between 396 eV and 398 eV. Gradually, the energy is distributed into a motion along the flat torsional coordinate, thereby reducing the amplitude of the bending and destroying the coherence (i.e. breaking the symmetry). This process is associated with a red-shift of the $1s \rightarrow \pi^*$ transition. The loss of coherence with respect to the bending coordinate is expected to introduce a slight broadening of the peaks. Furthermore, with approaching the region of 90° torsion, the gap between the $1s \rightarrow n$ and the $1s \rightarrow \pi^*$ peaks will diminish to about 1-1.5 eV. In the region of 90° torsion azobenzene becomes subject to a gradient towards strong asymmetric distortion along the bending coordinate towards the CI seam. As seen in Figure 5(a) this would induce a merging and broadening of the transient absorption signal. Upon decay to the GS and ultrafast leaving of the crossing region our simulations suggest the decrease of signal intensity in the 400 eV spectral window. Instead, the oscillatory motion of the GS wave packet along the torsional degree of freedom would translate into an oscillatory $1s \rightarrow \pi^*$ spectral dynamics between 397 eV and 398.5 eV. However, this feature might be obscured by the considerable broadening expected due to the vibrational dynamics along the coordinate exhibiting very different values for CNN and NNC bending angles.

4 Conclusion

We have shown here how time resolved NEXAFS can be applied to study transient dynamics of UV-excited molecules, as its signals are sensitive to specific geometrical changes along the reactive coordinates.

The main results here reported are the following: i) large geometrical deformations not necessarily translate in large differences in the NEXAFS spectra, which are instead sensitive to displacements along coordinates which affect the valence orbitals of the bright core-to-valence transitions; ii) the relevant coordinates, which describe the isomerization dynamics on the $n\pi^*$ state provide, respectively: a blue shift of the $1s \rightarrow n$ transition (symmetric bending), a core specific blue-shift of the signals accompanied by a pronounced broadening (asymmetric bending), and a red-shift of the $1s \rightarrow \pi^*$ transition (torsion), as summarized in Figure 3.

	Peak label[a]	Main Config.	Weight	Energy (PT2)	$\lvert TDM \rvert^2$	Peak label	Main Config.	weight	Energy (PT2)	$\lvert TDM \rvert^2$
		MEP 1					MEP 2			
GS - NEXAFS	-	$1s^{[1]}n^{[2]}\pi^{*[1]}$	0.89	398.4	4.98×10^{-3}	-	$1s^{[1]}n^{[2]}\pi^{*[1]}$	0.88	398.4	4.97×10^{-3}
$n\pi^*$ - NEXAFS	-	$1s^{[1]}n^{[2]}\pi^{*[1]}$	0.89	395.9	2.46×10^{-3}	-	$1s^{[1]}n^{[2]}\pi^{*[1]}$	0.88	396.4	2.64×10^{-3}
	-	$1s^{[1]}n^{[1]}\pi^{*[2]}$	0.90	399.1	2.42×10^{-3}	-	$1s^{[1]}n^{[1]}\pi^{*[2]}$	0.90	399.2	2.41×10^{-3}
		MEP 3					MEP 4			
GS - NEXAFS	-	$1s^{[1]}n^{[2]}\pi^{*[1]}$	0.88	398.4	4.96×10^{-3}	-	$1s^{[1]}n^{[2]}\pi^{*[1]}$	0.88	398.0	4.68×10^{-3}
$n\pi^*$ - NEXAFS	-	$1s^{[1]}n^{[2]}\pi^{*[1]}$	0.88	396.7	2.67×10^{-3}	-	$1s^{[1]}n^{[2]}\pi^{*[1]}$	0.88	396.8	2.46×10^{-3}
	-	$1s^{[1]}n^{[1]}\pi^{*[2]}$	0.71	399.1	1.61×10^{-3}	-	$1s^{[1]}n^{[1]}\pi^{*[2]}$	0.64	398.9	2.23×10^{-3}
		MEP 5					MEP 6			
GS - NEXAFS	-	$1s^{[1]}n^{[2]}\pi^{*[1]}$	0.89	397.7	4.44×10^{-3}	-	$1s^{[1]}n^{[2]}\pi^{*[1]}$	0.89	397.3[b]	3.65×10^{-3}
						-	$1s^{[1]}n^{[1]}\pi^{*[2]}$	0.84	399.1[b]	1.33×10^{-3}
$n\pi^*$ - NEXAFS	-	$1s^{[1]}n^{[2]}\pi^{*[1]}$	0.89	396.8	2.21×10^{-3}	-	$1s^{[1]}n^{[2]}\pi^{*[1]}$	0.89	396.8[b]	1.93×10^{-3}
	-	$1s^{[1]}n^{[1]}\pi^{*[2]}$	0.72	398.8	2.60×10^{-3}	-	$1s^{[1]}n^{[1]}\pi^{*[2]}$	0.84	398.6[b]	2.65×10^{-3}
		MEP 8 (core 1)					MEP 8 (core 2)			
GS - NEXAFS	-	$1s^{[1]}n^{[1]}\pi^{*[2]}$	0.86	397.7	4.09×10^{-3}	-	$1s^{[1]}n^{[2]}\pi^{*[1]}$	397.4	0.89	4.25×10^{-3}
$n\pi^*$ - NEXAFS	-	$1s^{[1]}n^{[1]}\pi^{*[2]}$	0.86	398.5	5.45×10^{-3}	-	$1s^{[1]}n^{[2]}\pi^{*[1]}$	0.89	396.9	4.11×10^{-3}
		MEP 7 (core 1)					MEP 7 (core 2)			
GS - NEXAFS	-	$1s^{[1]}n^{[2]}\pi^{*[1]}$	0.89	397.4[b]	3.41×10^{-3}	-	$1s^{[1]}n^{[2]}\pi^{*[1]}$	0.89	397.0[b]	3.87×10^{-3}
$n\pi^*$ - NEXAFS	-	$1s^{[1]}n^{[1]}\pi^{*[2]}$	0.79	399.1[b]	4.68×10^{-3}	-	$1s^{[1]}n^{[2]}\pi^{*[1]}$	0.89	397.5[b]	3.93×10^{-3}

Table 3 Report of the properties of the main peaks observed in Figure 6: configurations with the highest weight, RASSCF and RASPT2 energies (in eV), and the module squared of the transition dipole moment (in a.u.^{2}). [a] The peak labels refer to those of Figure 6. [b] These values are obtained after the MSPT2 unmixing of the first three valence Roots.

The dynamics along the minimum energy path (Figure 6), characterized by the following evolution along symmetric bending, torsion, and asymmetric bending, leads to the progressive merging of the $1s \rightarrow \pi^*$ and $1s \rightarrow n$ signals, which reach the maximal overlap in the vicinity of the conical intersection seam. This feature promises a way to spot movement towards, and passage through, the crossing seam in transient absorption experiments. We note that significant broadening of the bands due to the ultrashort core-to-valence state lifetime, does not impair the analysis.

We remark the fact that, in the present contribution, we focused on the analysis of the signals of a single molecule at different geometries along the MEP, while an average over an ensemble of trajectory is necessary to simulate a realistic spectrum. This averaging over many trajectories translates in an averaging of signals coming from different regions of the PES, and may therefore result in a partial obscuring of some of the features. Furthermore, as in real experiments the optical pump pulse excites only a fraction of the molecules in the sample, NEXAFS spectra record a superposition of the excited state (minor fraction) and the ground-state (major fraction) absorption spectra. This requires the difference in the GS- and ES-NEXAFS spectra to be sufficiently large to be detected, as is the case with the $1s \rightarrow n$ transition. Therefore, our analysis suggests that the best suited molecular targets for X-ray mapping should be organic molecules containing hereroatoms with electron lone pairs (like nucleobases, amino acids, and azoswitches) which are characterized by a coherent ballistic motion of a compact wave packet from the FC point to the CI region.

5 Conflicts of interest

There are no conflicts to declare.

Acknowledgements

M.G., F.S., A.N. and S.M. acknowledge support from the Chemical Sciences, Geosciences, and Bio-sciences division, Office of Basic Energy Sciences, Office of Science, U.S. Department of Energy, through award No. DE-SC0019484.

References

1 W. Ackermann, G. Asova, V. Ayvazyan, A. Azima, N. Baboi, J. Bähr, V. Balandin, B. Beutner, A. Brandt, A. Bolzmann, R. Brinkmann, O. I. Brovko, M. Castellano, P. Castro, L. Catani, E. Chiadroni, S. Choroba, A. Cianchi, J. T. Costello, D. Cubaynes, J. Dardis, W. Decking, H. Delsim-Hashemi, A. Delserieys, G. D. Pirro, M. Dohlus, S. Düsterer, A. Eckhardt, H. T. Edwards, B. Faatz, J. Feldhaus, K. Flöttmann, J. Frisch, L. Fröhlich, T. Garvey, U. Gensch, C. Gerth, M. Görler, N. Golubeva, H.-J. Grabosch, M. Grecki, O. Grimm, K. Hacker, U. Hahn, J. H. Han, K. Honkavaara, T. Hott, M. Hüning, Y. Ivanisenko, E. Jaeschke, W. Jalmuzna, T. Jezynski, R. Kammering, V. Katalev, K. Kavanagh, E. T. Kennedy, S. Khodyachykh, K. Klose, V. Kocharyan, M. Körfer, M. Kollewe, W. Koprek, S. Korepanov, D. Kostin, M. Krassilnikov, G. Kube, M. Kuhlmann, C. L. S. Lewis, L. Lilje, T. Limberg, D. Lipka, F. Löhl, H. Luna, M. Luong, M. Martins, M. Meyer, P. Michelato, V. Miltchev, W. D. Möller, L. Monaco, W. F. O. Müller, O. Napieralski, O. Napoly, P. Nicolosi, D. Nölle, T. Nuñez, A. Oppelt, C. Pagani, R. Paparella, N. Pchalek, J. Pedregosa-Gutierrez, B. Petersen, B. Petrosyan, G. Petrosyan, L. Petrosyan, J. Pflüger, E. Plönjes, L. Poletto, K. Pozniak, E. Prat, D. Proch, P. Pucyk, P. Radcliffe, H. Redlin, K. Rehlich, M. Richter, M. Roehrs, J. Roensch,

R. Romaniuk, M. Ross, J. Rossbach, V. Rybnikov, M. Sachwitz, E. L. Saldin, W. Sandner, H. Schlarb, B. Schmidt, M. Schmitz, P. Schmüser, J. R. Schneider, E. A. Schneidmiller, S. Schnepp, S. Schreiber, M. Seidel, D. Sertore, A. V. Shabunov, C. Simon, S. Simrock, E. Sombrowski, A. A. Sorokin, P. Spanknebel, R. Spesyvtsev, L. Staykov, B. Steffen, F. Stephan, F. Stulle, H. Thom, K. Tiedtke, M. Tischer, S. Toleikis, R. Treusch, D. Trines, I. Tsakov, E. Vogel, T. Weiland, H. Weise, M. Wellhöfer, M. Wendt, I. Will, A. Winter, K. Wittenburg, W. Wurth, P. Yeates, M. V. Yurkov, I. Zagorodnov and K. Zapfe, *Nature Photonics*, 2007, **1**, 336–342.

2 P. Emma, R. Akre, J. Arthur, R. Bionta, C. Bostedt, J. Bozek, A. Brachmann, P. Bucksbaum, R. Coffee, F.-J. Decker, Y. Ding, D. Dowell, S. Edstrom, A. Fisher, J. Frisch, S. Gilevich, J. Hastings, G. Hays, P. Hering, Z. Huang, R. Iverson, H. Loos, M. Messerschmidt, A. Miahnahri, S. Moeller, H.-D. Nuhn, G. Pile, D. Ratner, J. Rzepiela, D. Schultz, T. Smith, P. Stefan, H. Tompkins, J. Turner, J. Welch, W. White, J. Wu, G. Yocky and J. Galayda, *Nature Photonics*, 2010, **4**, 641–647.

3 T. Ishikawa, H. Aoyagi, T. Asaka, Y. Asano, N. Azumi, T. Bizen, H. Ego, K. Fukami, T. Fukui, Y. Furukawa, S. Goto, H. Hanaki, T. Hara, T. Hasegawa, T. Hatsui, A. Higashiya, T. Hirono, N. Hosoda, M. Ishii, T. Inagaki, Y. Inubushi, T. Itoga, Y. Joti, M. Kago, T. Kameshima, H. Kimura, Y. Kirihara, A. Kiyomichi, T. Kobayashi, C. Kondo, T. Kudo, H. Maesaka, X. M. Maréchal, T. Masuda, S. Matsubara, T. Matsumoto, T. Matsushita, S. Matsui, M. Nagasono, N. Nariyama, H. Ohashi, T. Ohata, T. Ohshima, S. Ono, Y. Otake, C. Saji, T. Sakurai, T. Sato, K. Sawada, T. Seike, K. Shirasawa, T. Sugimoto, S. Suzuki, S. Takahashi, H. Takebe, K. Takeshita, K. Tamasaku, H. Tanaka, R. Tanaka, T. Tanaka, T. Togashi, K. Togawa, A. Tokuhisa, H. Tomizawa, K. Tono, S. Wu, M. Yabashi, M. Yamaga, A. Yamashita, K. Yanagida, C. Zhang, T. Shintake, H. Kitamura and N. Kumagai, *Nature Photonics*, 2012, **6**, 540–544.

4 M. Kowalewski, B. P. Fingerhut, K. E. Dorfman, K. Bennett and S. Mukamel, *Chemical Reviews*, 2017, **117**, 12165–12226.

5 M. Kowalewski, K. Bennett and S. Mukamel, *Structural Dynamics*, 2017, **4**, 054101.

6 J. R. Rouxel, Y. Zhang and S. Mukamel, *Chemical Science*, 2019, **10**, 898–908.

7 M. Gühr, *Synchrotron Radiation News*, 2016, **29**, 8–12.

8 J. Stöhr, *NEXAFS Spectroscopy*, Springer Berlin Heidelberg, 1992.

9 *X-Ray Absorption and X-Ray Emission Spectroscopy*, ed. J. A. V. Bokhoven and C. Lamberti, John Wiley & Sons, Ltd, 2016.

10 C. Bressler and M. Chergui, *Annual Review of Physical Chemistry*, 2010, **61**, 263–282.

11 P. Wernet, K. Kunnus, I. Josefsson, I. Rajkovic, W. Quevedo, M. Beye, S. Schreck, S. Grübel, M. Scholz, D. Nordlund, W. Zhang, R. W. Hartsock, W. F. Schlotter, J. J. Turner, B. Kennedy, F. Hennies, F. M. F. de Groot, K. J. Gaffney, S. Techert, M. Odelius and A. Föhlisch, *Nature*, 2015, **520**, 78–81.

12 A. R. Attar, A. Bhattacherjee, C. D. Pemmaraju, K. Schnorr, K. D. Closser, D. Prendergast and S. R. Leone, *Science*, 2017, **356**, 54–59.

13 T. J. A. Wolf, R. H. Myhre, J. P. Cryan, S. Coriani, R. J. Squibb, A. Battistoni, N. Berrah, C. Bostedt, P. Bucksbaum, G. Coslovich, R. Feifel, K. J. Gaffney, J. Grilj, T. J. Martinez, S. Miyabe, S. P. Moeller, M. Mucke, A. Natan, R. Obaid, T. Osipov, O. Plekan, S. Wang, H. Koch and M. Gühr, *Nature Communications*, 2017, **8**, year.

14 P. A. Malmqvist, A. Rendell and B. O. Roos, *The Journal of Physical Chemistry*, 1990, **94**, 5477–5482.

15 K. Andersson, P. A. Malmqvist, B. O. Roos, A. J. Sadlej and K. Wolinski, *J. Phys. Chem.*, 1990, **94**, 5483–5488.

16 V. Sauri, L. S. Andres, A. R. M. Shahi, L. Gagliardi, S. Vancoillie and K. Pierloot, *J. Chem. Theory Comput.*, 2011, **7**, 153.

17 C. Ehlert, M. Gühr and P. Saalfrank, *The Journal of Chemical Physics*, 2018, **149**, 144112.

18 D. Polli, P. Altoè, O. Weingart, K. M. Spillane, C. Manzoni, D. Brida, G. Tomasello, G. Orlandi, P. Kukura, R. A. Mathies, M. Garavelli and G. Cerullo, *Nature*, 2010, **467**, 440–443.

19 B. O. Roos, *Ab Initio Methods in Quantum Chemistry: Part II*, Wiley, Chicester, UK, 1987.

20 B. O. Roos, P. R. Taylor and P. E. M. Siegbahn, *Chem. Phys.*, 1980, **48**, 157.

21 D. Roca-Sanjuán, F. Aquilante and R. Lindh, *Wiley Interdisciplinary Reviews: Computational Molecular Science*, 2011, **2**, 585–603.

22 J. Norell, R. M. Jay, M. Hantschmann, S. Eckert, M. Guo, K. J. Gaffney, P. Wernet, M. Lundberg, A. Föhlisch and M. Odelius, *Physical Chemistry Chemical Physics*, 2018, **20**, 7243–7253.

23 I. Josefsson, K. Kunnus, S. Schreck, A. Föhlisch, F. de Groot, P. Wernet and M. Odelius, *The Journal of Physical Chemistry Letters*, 2012, **3**, 3565–3570.

24 W. Hua, S. Oesterling, J. D. Biggs, Y. Zhang, H. Ando, R. de Vivie-Riedle, B. P. Fingerhut and S. Mukamel, *Structural Dynamics*, 2015, **3**, 023601.

25 F. Aquilante, J. Autschbach, R. K. Carlson, L. F. Chibotaru, M. G. Delcey, L. D. Vico, I. F. Galván, N. Ferré, L. M. Frutos, L. Gagliardi, M. Garavelli, A. Giussani, C. E. Hoyer, G. L. Manni, H. Lischka, D. Ma, P. Å. Malmqvist, T. Müller, A. Nenov, M. Olivucci, T. B. Pedersen, D. Peng, F. Plasser, B. Pritchard, M. Reiher, I. Rivalta, I. Schapiro, J. Segarra-Martí, M. Stenrup, D. G. Truhlar, L. Ungur, A. Valentini, S. Vancoillie, V. Veryazov, V. P. Vysotskiy, O. Weingart, F. Zapata and R. Lindh, *Journal of Computational Chemistry*, 2015, **37**, 506–541.

26 M. Lundberg and M. G. Delcey, *Transition Metals in Coordination Environments*, Springer International Publishing, 2019.

27 T. Fleig, J. Olsen and L. Visscher, *The Journal of Chemical Physics*, 2003, **119**, 2963–2971.

28 D. Ma, G. L. Manni and L. Gagliardi, *The Journal of Chemical Physics*, 2011, **135**, 044128.

29 M. Guo, L. K. Sørensen, M. G. Delcey, R. V. Pinjari and M. Lundberg, *Physical Chemistry Chemical Physics*, 2016, **18**, 3250–3259.

30 E. Ertan, V. Savchenko, N. Ignatova, V. V. da Cruz, R. C. Couto,

S. Eckert, M. Fondell, M. Dantz, f. A. P. Brian Kennedy, e Thorsten Schmitt, A. Frölich, F. GelâĂŹmukhanov, M. Odelius and V. Kimberg, *Phys. Chem. Chem. Phys.*, 2018, **20**, 14384.

31 G. Ghigo, B. O. Roos and P. Malmqvist, *Chem. Phys. Lett.*, 2004, **396**, 142 – 149.

32 N. Forsberg and P. Malmqvist, *Chem. Phys. Lett.*, 1997, **274**, 196 – 204.

33 B. O. Roos, V. Veryazov and P.-O. Widmark, *Theor. Chem. Acc.*, 345, **11**, 2004.

34 F. Aquilante, T. B. Pedersen and R. Lindh, *Theor. Chem. Acc.*, 2009, **124**, 1.

35 F. Aleotti, L. Soprani, A. Nenov, R. Berardi, C. Zannoni and M. Garavelli, *Submitted*, 2019.

36 R. Manne, *The Journal of Chemical Physics*, 1970, **52**, 5733–5739.

37 J. Casellas, M. J. Bearpark and M. Reguero, *ChemPhysChem*, 2016, **17**, 3068–3079.

38 A. Nenov, R. Borrego-Varillas, A. Oriana, L. Ganzer, F. Segatta, I. Conti, J. Segarra-Marti, Omachi, J., M. Dapor, S. Taioli, C. Manzoni, S. Mukamel, G. Cerullo and M. Garavelli, *J. Phys. Chem. Lett.*, 2018, **9**, 1534–1541.